Communications on Applied Nonlinear Analysis
ISSN: 1074-133X
Vol 33 No. 1s (2026)

Lamb Wave-Based Nondestructive Evaluation of Voided Adhesive Interfaces Using Chebyshev Spectral Dispersion Modeling

M.S.L.R.Mallika[1], G.Sudheer[2], N.Aparna[3]

[1] Dept. of Mathematics, Anil Neerukonda Institute of Technology & Sciences, Visakhapatnam, AP

[2] Dept. of Mathematics, GVP College of Engineering for Women, Visakhapatnam, AP

[3] Earth & Climate Sciences Area, National Remote Sensing Centre, Hyderabad, Telengana

Corresponding author email id: sudhwave@gmail.com

Article History:

Received:12-01-2026

Revised:05-02-2026

Accepted:04-03-2026

Abstract:

A reformulated model for Lamb wave propagation in an aluminium/adhesive/aluminium sandwich plate is presented, where the adhesive core is described using the theory of Linear Elastic Materials with Voids (LEMV). A Chebyshev spectral collocation scheme is employed to assemble, at prescribed real wavenumbers γ, the generalized eigenvalue problem K(γ)v=ω^2 Mv. This approach enables computation of the complete set of propagating branches without sequential mode-tracking and incorporates the porosity field φ as an additional kinematic variable within the coupled formulation.

To reduce reliance on phenomenological parameter selection, the LEMV coefficients associated with porosity are related to the measurable void volume fraction f of the adhesive through a microstructure-informed calibration procedure. Dispersion relations and corresponding group velocity curves v_g=∂ω/∂γ are computed from the resulting eigenstructure. Zero Group Velocity (ZGV) points are identified and examined as functions of f. The results indicate systematic variations of selected ZGV frequencies with increasing void fraction, suggesting their potential relevance for quantitative nondestructive evaluation of bonded interfaces, within the assumptions of the present LEMV framework.

Keywords: Lamb waves; composite plates; linear elastic material with voids; Chebyshev spectral collocation; dispersion; group velocity; zero group velocity resonances; nondestructive evaluation; porosity characterization; void volume fraction.

MSC 2020: 74J05, 74B05, 74A60, 65N25

1. Introduction

Adhesively bonded composite laminates are central to aerospace, automotive, and civil structural applications. The quality of the adhesive bond is critically sensitive to the

microscopic state of the interface: distributed voids, pores, and minute separations arise during curing and in service, weakening the effective mechanical coupling between the adherends. Guided elastic wave methods—particularly Lamb waves—offer a non-contact, whole-field probe of bond integrity and have seen increasing application in nondestructive evaluation (NDE) of composite structures.

Vasudeva and Govinda Rao [1] proposed a physically motivated continuum model in which the thin adhesive layer at the core of a symmetric sandwich plate is treated as a Linear Elastic Material with Voids (LEMV) in the sense of Cowin and Nunziato [2]. From a theoretical standpoint, LEMV is the simplest special case of Mindlin's theory of media with microstructure, obtained by restricting the micro-deformation tensor to spherical form so that a single scalar field—the micro-dilatation ϕ—is the only kinematic variable beyond the displacement field [3]. This restriction also implies that, for centrosymmetric materials, the porosity field couples exclusively to volumetric (dilatational) deformation and is completely decoupled from shear, a property that has important consequences for the selective sensitivity of different Lamb-wave families to void content. In this theory the bulk density ρ of the voided material equals the product of the matrix material density γ_m and a volume-fraction field $v \in [0,1]$:

$$\rho = \gamma_m \, v. \tag{1}$$

A change ϕ in volume fraction from the reference value acts as an additional kinematic variable, governed by its own balance equation and coupled to the elastic displacement field through a coupling modulus β. This introduces two additional wave speeds beyond the classical compressional and shear speeds, and a dimensionless void coupling parameter

$$N = \frac{\beta^2}{\xi\,(\lambda^c + 2\mu^c)}, \qquad 0 \le N < N_{\max} = \frac{1+\nu^c}{3(1-\nu^c)}, \tag{2}$$

that controls how strongly the porosity field influences the elastic wave motion. Increasing N simulates a more voided, weaker bond.

The original paper [1] derived exact 7×7 determinantal frequency equations and compared dispersion curves with the adhesive-layer model of Mal, Xu, and Bar-Cohen [4], the harmonic sandwich plate theory of Lee and Chang [5], and the linear slip interface model of Schoenberg [6] for an Al/adhesive/Al sandwich, showing qualitatively consistent trends. However, the authors themselves identified two significant drawbacks based on the experimental works available at that time: *"The first is that the velocities V_3^c and V_4^c used are hypothetical because no real materials, especially adhesives, are known so far to belong to the class of materials described by the theory of LEMV, and as such ω_0, l_0, l_1, l_2, and N remain hypothetical."*

This paper attempts to address the shortcomings based on the progress observed in the literature on experimental works related to the problem carried out in recent years. The numerical method is upgraded from determinant root-finding to Chebyshev spectral collocation, and the LEMV parameters are grounded in a computational microstructure-matching methodology [7] that provides empirical fits $\beta(f)$, $N(f)$, and $\xi(f)$ as functions of the measurable void volume fraction f of the adhesive. The coupling number fit is further recalibrated from the Bishay reference Poisson ratio $\nu_B = 0.3$ to the adhesive value $\nu^c = 1/3$ via a proportional rescaling of the amplitude coefficients, completing the parameter map for $N = 0.66$. The resulting physically parameterized dispersion model is then extended to

compute group velocity curves and to identify and analyze Zero Group Velocity (ZGV) resonances, which had not been previously considered in the LEMV context.

ZGV Lamb modes, the points $(\gamma_{ZGV}, \omega_{ZGV})$ on a dispersion branch where $\partial\omega/\partial\gamma = 0$ at $\gamma_{ZGV} \neq 0$, generate spatially localized, frequency-selective resonances. They produce distinct spectral peaks in broadband plate-wave spectra and are detectable by laser Doppler vibrometry or air-coupled transducers without contact [8]. At a ZGV point the integral of the acoustic power flux across the plate cross-section is identically zero [9], meaning elastic energy cannot propagate away from the source; this leads to strong, long-lived resonances whose temporal decay begins with a power-law $t^{-1/2}$ phase (geometric spreading from finite source size) before transitioning to an exponential decay governed by material damping [9]. The ZGV resonance frequency is set by a competition between two cut-off frequencies of the same modal symmetry—one that is independent of interface properties and one that shifts with interfacial coupling—a repulsion mechanism first identified for single plates [8] and recently demonstrated experimentally for bilayer structures bonded by thin interlayers [10]. Because the ZGV frequencies are sensitive to the material and geometric parameters of the system, and because N (and hence f) now has a traceable physical meaning via the Bishay calibration, the ZGV spectrum constitutes a quantitative NDE signature for void content in composite adhesive bonds. Critically, a one-to-one correspondence exists between ZGV frequencies and interfacial coupling parameters [10], so that any experimentally measured ZGV frequency directly yields a unique estimate of f.

2. LEMV Theory and Governing Equations

2.1 Geometry

A right-handed Cartesian coordinate system (x_1, x_2, x_3) is adopted. The x_1-axis is aligned with the direction of wave propagation in the plane of the plate; the x_2-axis is directed normal to the plate mid-plane and is taken as the thickness direction; and the x_3-axis lies in the plate plane orthogonal to the propagation direction, completing the right-handed triad. The plate is assumed infinite in the x_1–x_3 plane, so that all field quantities depend only on x_2 and the propagation coordinate x_1 (and on time t), reducing the problem to a two-dimensional one in the x_1–x_2 plane.

The sandwich consists of two aluminium facings of thickness t^f bonded symmetrically about the mid-plane $x_2 = 0$. Each facing occupies the region $t^c < |x_2| < t^c + t^f$, and the LEMV adhesive core of half-thickness t^c occupies the central region $|x_2| < t^c$. The total plate half-thickness is therefore $t^c + t^f$, and the full plate thickness is $h_{tot} = 2(t^c + t^f)$. Superscripts f and c denote quantities belonging to the facing and core sub-domains, respectively.

2.2 Kinematic Variables and Micro-Dilatation

The LEMV theory generalizes classical linear elasticity by elevating the local void volume fraction to an independent kinematic field rather than treating porosity as a fixed material constant. This is the fundamental distinction between the present model and a conventional elastic sandwich plate: the adhesive core carries not only displacement degrees of freedom but also a scalar micro-dilatation field that tracks the departure of the void volume fraction from its reference value at every material point and instant. Following the formulation of Cowin and Nunziato [2] and Bishay et al. [7], the independent kinematic variables in the LEMV core are the displacement field u_i^c and the micro-dilatation (change in matrix volume fraction from the reference state):

$$\phi = \Psi(x,t) - \Psi_0(x,t); \qquad \Psi = \frac{V_{\text{matrix}}}{V}, \quad \Psi_0 = \frac{V^R_{\text{matrix}}}{V}, \tag{3}$$

where $-1 < \phi < 1$. The volume fraction of voids (porosity) is related to ϕ by

$$f_{\text{current}} = f_{\text{reference}} - \phi. \tag{4}$$

The strain tensor is $\varepsilon_{ij} = \frac{1}{2}\left(u_{i,j} + u_{j,i}\right)$ and the gradient of micro-dilatation is $\psi_i = \phi_{,i}$.

2.3 Constitutive Equations

The LEMV constitutive relations generalize Hooke's law by coupling the Cauchy stress tensor to the micro-dilatation field through the porosity change stress parameter β. Three constitutive equations are required in place of the single stress-strain law of classical elasticity: one for the Cauchy stress τ^c_{ij}, one for the equilibrated stress vector h_i associated with the spatial gradient of ϕ, and one for the intrinsic equilibrated body force g that governs the temporal evolution of the void volume fraction. The scalar g plays the role of a restoring force that drives ϕ back toward its reference value whenever the void field is disturbed by elastic deformation. All three constitutive equations can be derived from the quadratic strain energy density [2,3]

$$U = \frac{1}{2}\lambda^c(\varepsilon^c_{kk})^2 + \mu^c e^c_{ij} e^c_{ij} + \beta\,\phi\,\varepsilon^c_{kk} + \frac{1}{2}\xi\,\phi^2 + \frac{1}{2}\alpha\,\phi_{,k}\phi_{,k} \tag{5}$$

by differentiation with respect to the appropriate strain measures. Positivity of U for all admissible strain states requires, in addition to the usual conditions $\lambda^c + 2\mu^c/3 > 0$ and $\mu^c > 0$, the constraint

$$\beta^2 < \left(\lambda^c + \frac{2}{3}\mu^c\right)\xi \tag{5a}$$

which is precisely the condition that bounds the coupling number: $N = \beta^2/[\xi(\lambda^c + 2\mu^c)] < N_{\max} < 1$. Equation (5a) is therefore not a modelling assumption but a thermodynamic necessity; any calibrated parameter set that violates it would predict unbounded growth of elastic energy and is physically inadmissible [3]. For the LEMV core [2,7]:

$$\tau^c_{ij} = \lambda^c \vartheta^c \delta_{ij} + 2\mu^c e^c_{ij} + \beta\,\delta_{ij}\,\phi \tag{6a}$$

$$h_i = \alpha\,\phi_{,i} \tag{6b}$$

$$g = -\omega_0\,\dot{\phi} - \xi\,\phi - \beta\,\varepsilon^c_{kk}. \tag{6c}$$

Here β is the porosity change stress parameter (coupling elastic stress to void volume change), ξ is the void stiffness coefficient, α is a diffusion coefficient, and ω_0 characterizes viscous dissipation in the pores. The viscoelastic extension of this framework is discussed by Cowin [11]; thermodynamic constraints on the LEMV free energy and energy dissipation inequalities are analyzed by Passmann [12]. For the aluminium facings the constitutive law reduces to classical linear elasticity:

$$\tau^f_{ij} = \lambda^f \vartheta^f \delta_{ij} + 2\mu^f e^f_{ij}. \tag{7}$$

2.4 Equations of Motion

Substituting the constitutive relations of Section 2.3 into the linear momentum balance and the equilibrated inertia balance yields a set of coupled partial differential equations in each sub-domain. The aluminium facings, being classically elastic, satisfy the standard Navier equation of motion in terms of the displacement field alone. The LEMV core requires two coupled equations: the elastic momentum equation, in which the micro-dilatation gradient $\nabla\phi$ acts as a body-force-like source term through the coupling modulus β, and the micro-dilatation balance equation, which governs the dynamics of the porosity field and is driven in turn by the volumetric strain $\nabla \cdot \mathbf{U}^c$. The two core equations are therefore inseparable and must be solved simultaneously.

Facings:

$$\mu^f \nabla^2 \mathbf{U}^f + (\lambda^f + \mu^f)\nabla\nabla \cdot \mathbf{U}^f = \rho^f \ddot{\mathbf{U}}^f, \qquad t^c < |x_2| < t^c + t^f. \tag{8}$$

LEMV core — elastic momentum:

$$\mu^c \nabla^2 \mathbf{U}^c + (\lambda^c + \mu^c)\nabla\nabla \cdot \mathbf{U}^c + \beta\, \nabla\phi = \rho^c \ddot{\mathbf{U}}^c, \qquad |x_2| < t^c. \tag{9}$$

LEMV core — micro-dilatation balance:

$$\alpha\, \nabla^2\phi - \omega_0\, \dot{\phi} - \xi\, \phi - \beta\, \nabla \cdot \mathbf{U}^c = \rho^c \kappa\, \ddot{\phi}, \qquad |x_2| < t^c. \tag{10}$$

The equilibrated inertia coefficient is $\kappa = \alpha l_2^2/(\rho^c {V_3^c}^2)$ where $l_2 = \sqrt{\alpha/\xi}$ is the void diffusion length and V_3^c is the secondary compressional speed in the LEMV material.

2.5 Wave Speeds

The dispersion characteristics of the sandwich plate are governed by four distinct characteristic wave speeds: two in the aluminium facings and four in the LEMV adhesive core. The facing speeds are the familiar compressional and shear speeds of classical linear elasticity and carry no dependence on the void fraction. The LEMV core supports two additional speeds, V_3^c and V_4^c, that arise exclusively from the micro-dilatation balance equation; it is the presence of these extra speeds—and the resulting additional wave mode—that enriches the dispersion surface and creates the Zero Group Velocity points analyzed in Section 5. The classical speeds in each region are:

$$V_1^f = \sqrt{(\lambda^f + 2\mu^f)/\rho^f}, \qquad V_2^f = \sqrt{\mu^f/\rho^f}; \tag{11a}$$

$$V_1^c = \sqrt{(\lambda^c + 2\mu^c)/\rho^c}, \qquad V_2^c = \sqrt{\mu^c/\rho^c}. \tag{11b}$$

The two additional LEMV speeds are:

$$V_3^c = \sqrt{\alpha^*/\kappa^*}, \qquad V_4^c = \frac{2\alpha}{l_0\, \omega}, \tag{11c}$$

where $\alpha^* = \alpha/\xi \equiv l_2^2$, $\kappa^* = \rho^c\kappa/\xi$, and $l_0 = l_1 l_2/\sqrt{l_1^2 - l_2^2 H}$ with $l_1 = \sqrt{\alpha/\beta}$ and $H = \beta/(\lambda^c + 2\mu^c)$. The classification of plane waves in LEMV materials according to the magnitudes of these speeds was established by Chandrasekharaiah [13] for the single-plate case; Appendix B extends this classification to the present sandwich geometry using the Bishay parameter map.

2.6 Boundary and Interface Conditions

The boundary and interface conditions imposed on the system are as follows. Traction-free outer faces at $|x_2| = t^c + t^f$ require $\tau_{ij}^f n_j = 0$. Displacement continuity at $|x_2| = t^c$ gives $U_i^f = U_i^c$ for $i = 1,2$. Traction continuity at the same interface requires $\tau_{ij}^f n_j = \tau_{ij}^c n_j$ for $i, j = 1,2$. The void gradient condition at $|x_2| = t^c$ [14] is $h_i n_i = \alpha\, \phi_{,x_2} = 0$. Mid-plane symmetry at $x_2 = 0$ requires: for extensional modes, $\partial U_1^c / \partial x_2 = 0$, $U_2^c = 0$, $\partial \phi / \partial x_2 = 0$; and for flexural modes, $U_1^c = 0$, $\partial U_2^c / \partial x_2 = 0$, $\phi = 0$.

3. Microstructure-Grounded Characterization of LEMV Parameters

This section constitutes the most significant physical enhancement over the original paper. The methodology follows Bishay, Repka, Sladek, and Sladek [7]. Related computational studies of LEMV and micro-dilatation theory that inform the present approach include the penalized micro-dilatation formulation of Ramézani, Steeb, and Jeong [15], the mixed-collocation finite element analysis of Bishay et al. [16], the meshless MLPG study of Sladek, Sladek, Repka, and Bishay [17], and the lattice-to-continuum identification of all micro-dilatation constants (N, ℓ, β, ξ, α) for composite auxetic metamaterials by Solyaev, Lurie, and Ustenko [3]. The last study is particularly instructive: it demonstrates that the complete set of LEMV parameters can be uniquely recovered from lattice finite-element simulations of unit-cell structures—providing independent confirmation that the Bishay-type RVE and beam-bending procedure employed here is theoretically well-founded and not specific to the adhesive geometry.

3.1 The Fundamental Gap in the Original Model

Vasudeva and Govinda Rao [1] acknowledged that all LEMV-specific parameters—β, ξ, ω_0, l_0, l_1, l_2, and N—are hypothetical for real adhesive materials. They therefore treated N as a free parameter taking values $\{0.01, 0.33, 0.66\}$ without physical justification. Bishay et al. [7] fill this gap by providing a systematic two-step computational procedure to relate β, N, and ξ to the measurable void volume fraction f of the porous material and the elastic moduli of its matrix.

3.2 Void Volume Fraction and Microstructure Geometry

For a 2D porous medium with circular voids of radius r arranged on a square lattice with center-to-center spacing d, the reference void volume fraction is

$$f = \frac{n\,\pi r^2}{bL}, \tag{12}$$

where n is the number of voids in a domain of width b and length L. The radius corresponding to prescribed f and n is

$$r = \sqrt{\frac{f\,bL}{n\,\pi}}. \tag{13}$$

The micro-dilatation ϕ is related to the current void radius $r + \Delta r$ and the reference radius r by

$$\phi = f_{\text{ref}} - f_{\text{current}} = \frac{\pi r^2}{a^2} - \frac{\pi (r+\Delta r)^2}{a^2}, \tag{14}$$

where a is the side length of the Representative Volume Element (RVE).

3.3 Step 1 — Characterization of β via RVE Analysis

Consider a square RVE containing a single circular void. The outer boundaries are fixed (zero macroscopic strain) and the void radius is prescribed to change by Δr, imposing a known ϕ via Eq. (14). Under zero macroscopic strain the LEMV constitutive law (6a) reduces (under plane stress, using the plane-stress correction $\beta^* = [(1-2\nu)/(1-\nu)]\beta$) to

$$\beta^* = \frac{\bar{\sigma}_{11}+\bar{\sigma}_{22}}{2\phi}, \tag{15}$$

where $\bar{\sigma}_{ij} = A^{-1}\int_A \sigma_{ij}\, dA$ is the volume-averaged stress from the finite element solution of the RVE. The plane-stress correction from Bishay et al. [7] gives:

$$\beta = \frac{1-\nu}{1-2\nu}\,\beta^*. \tag{16}$$

Numerical RVE analyses over $f \in [0.05, 0.50]$ yield the cubic fit [7]:

$$\beta(f) = a_3 f^3 + a_2 f^2 + a_1 f + a_0 \tag{17}$$

with coefficients for matrix material $E = 2\times10^{11}$ Pa, $\nu = 0.3$:

$$a_3 = 1.0333\times10^{12}, \quad a_2 = -1.2726\times10^{11}, \quad a_1 = 3.0966\times10^{11},$$
$$a_0 = 2.4722\times10^{11}\ \text{[Pa]}.$$

Note that $\beta(f) \to \beta(0^+)$ is well-defined from the cubic fit as $f \to 0^+$ (with $N \to 0$ simultaneously), but the LEMV theory itself reduces to classical elasticity when $\phi \equiv 0$, so the coupling is inactive in a void-free material.

Adaptation for the adhesive core: Starting from the Lamé constants $\lambda^c = 0.828$ and $\mu^c = 0.414$ g·mm^{-1}·μs^{-2} (Table 1), the Poisson ratio and Young's modulus of the adhesive matrix are obtained as follows.

Table 1 — Material parameters (after Vasudeva and Govinda Rao [1]).

Layer	Material	t (mm)	ρ (g/cm^3)	V_1 (mm/μs)	V_2 (mm/μs)	V_3 (mm/μs)	V_4 (mm/μs)
Facings	Aluminium	0.965	2.8	6.4	3.1	—	—
Core	LEMV Adhesive	0.127	1.21	1.17	0.585	0.980	0.895

Derived elastic constants of the aluminium facings:

$$\mu^f = \rho^f\left(V_2^f\right)^2 = 26.908\ \text{g mm}^{-1}\,\mu\text{s}^{-2}, \qquad \lambda^f = \rho^f\left[\left(V_1^f\right)^2 - 2\left(V_2^f\right)^2\right] = 61.824\ \text{g mm}^{-1}\,\mu\text{s}^{-2}.$$

Derived elastic constants of the adhesive core matrix:

$$\mu^c = 0.414\ \text{g mm}^{-1}\,\mu\text{s}^{-2}, \qquad \lambda^c = 0.828\ \text{g mm}^{-1}\,\mu\text{s}^{-2}, \qquad l_2 = 0.005\ \text{mm}.$$

Poisson ratio. For an isotropic elastic solid, $\lambda = 2\mu\nu/(1-2\nu)$, which rearranges to

$$\nu^c = \frac{\lambda^c}{2(\lambda^c + \mu^c)} = \frac{0.828}{2(0.828 + 0.414)} = \frac{0.828}{2.484} = \frac{1}{3}.$$

Young's modulus. Using $E = 2\mu(1 + \nu)$:

$$E^c = 2\mu^c(1 + \nu^c) = 2 \times 0.414 \times \frac{4}{3} = 1.104 \text{ g·mm}^{-1}\text{·µs}^{-2} = 1.104 \text{ GPa}.$$

Modulus scaling. The Bishay [7] β-coefficients a_i were calibrated for a steel-like matrix with $E_B = 200$ GPa and $\nu_B = 0.3$. Because the RVE stresses scale linearly with E under fixed displacement boundary conditions, β scales proportionally:

$$\beta^c(f) = \frac{E^c}{E_B}\,\beta^B(f) \equiv s_E\,\beta^B(f), \qquad s_E = \frac{1.104}{200} = 5.521 \times 10^{-3}. \tag{18}$$

Applying this scaling to Eq. (17) yields the adhesive-specific cubic fit:

$$\beta^c(f) = a_3^c f^3 + a_2^c f^2 + a_1^c f + a_0^c \tag{19}$$

with coefficients

$$a_3^c = 5.705 \times 10^9, \quad a_2^c = -7.026 \times 10^8, \quad a_1^c = 1.710 \times 10^9, \quad a_0^c = 1.365 \times 10^9 \text{ [Pa]}.$$

Representative values are: $\beta^c(0.10) = 1.535$ GPa, $\beta^c(0.20) = 1.724$ GPa, $\beta^c(0.30) = 1.969$ GPa, growing monotonically with void content as expected. The β^c coefficients are valid for $\nu^c = 1/3$ without further modification, since the RVE boundary-value problem depends on ν only through the stress distribution, which is already accounted for by the modulus scaling s_E.

3.4 Step 2 — Characterization of N and ξ via Beam-Bending Calibration

A cantilever porous beam is analyzed by two parallel models: a microstructural model employing classical linear elasticity with all voids explicitly meshed, and a micro-dilatation model using a homogeneous LEMV domain with $\beta(f)$ from Eq. (19) and sweeping N. For each f, the value of N that matches the micro-dilatation beam-tip deflection to the microstructural model deflection is identified. Repeating over $f \in [0.05, 0.50]$ yields the exponential fit [7]:

$$N(f) = b_1 \exp(b_2 f) + b_3 \exp(b_4 f) \tag{20}$$

The Bishay calibration [7] was performed for the reference material with $\nu_B = 0.3$. Because the adhesive has $\nu^c = 1/3 \neq 0.3$, the amplitude coefficients must be rescaled to the adhesive (see Section 3.4a below); the recalibrated coefficients for $\nu^c = 1/3$ are:

$$b_1^c = 0.5180, \quad b_2^c = 0.4146, \quad b_3^c = -0.5163, \quad b_4^c = -21.36,$$

with $N^c(0) = b_1^c + b_3^c = 0.5180 - 0.5163 = 0.0017 \approx 0$ enforced (no voids ⇒ no coupling). The void stiffness coefficient follows from Eq. (2):

$$\xi^c(f) = \frac{[\beta^c(f)]^2}{N^c(f)\,(\lambda^c + 2\mu^c)} \tag{21}$$

where $\lambda^c + 2\mu^c = 0.828 + 2 \times 0.414 = 1.656$ g·mm^{-1}·µs^{-2} (= 1.656 GPa). Representative values of all three parameters for the adhesive are collected in Table 2.

The Bishay c_i coefficients for ξ (calibrated for $E_B = 200$ GPa, $\nu_B = 0.3$) are not directly transferred here; $\xi^c(f)$ is computed freshly from Eq. (21) using the rescaled $\beta^c(f)$ and the adhesive M^c.

3.4a Recalibration of $N(f)$ for $\nu^c = 1/3$

The maximum coupling number $N_{\max}$ depends solely on the matrix Poisson ratio through Eq. (2):

$$N_{\max} = \frac{1+\nu}{3(1-\nu)}. \quad (22)$$

This gives two distinct ceilings:

Material	ν	$N_{\max}$
Bishay reference (steel-like)	0.3	$\frac{13}{21} \approx 0.6190$
Adhesive core	$\frac{1}{3}$	$\frac{2}{3} \approx 0.6667$

Because $N(f)$ is controlled by the ratio of void-coupling energy to elastic compression energy, and because this ratio scales with $N_{\max}$ which depends solely on ν, the recalibrated function satisfies

$$N^c(f) = \frac{N^c_{\max}}{N^B_{\max}} N^B(f) = \frac{2/3}{13/21} N^B(f) = \frac{14}{13} N^B(f), \quad (23)$$

where the proportionality constant is $\eta = 14/13 \approx 1.0769$. The two exponential rate constants b_2 and b_4 govern the *rate of increase* of N with f, which depends on void geometry and on how quickly void volume fraction converts into volumetric coupling; this rate is insensitive to the 3.3 percentage-point difference in ν, so $b_2^c = b_2 = 0.4146$ and $b_4^c = b_4 = -21.36$ are retained unchanged.

The recalibrated amplitude coefficients are therefore $b_1^c = \eta\, b_1 = 1.0769 \times 0.481 = 0.5180$ and $b_3^c = \eta\, b_3 = 1.0769 \times (-0.4794) = -0.5163$, representing a uniform $+7.7\%$ increase in both amplitudes. The residual second-order uncertainty from applying the proportional rescaling rather than repeating the full Bishay FEA calibration at $\nu^c = 1/3$ is of order $(\Delta\nu/\nu_B)^2 \approx 1\%$, well within the modelling uncertainty of the original calibration. Thermodynamic admissibility is guaranteed analytically by construction: since $N^c(f) = \eta\, N^B(f) < \eta\, N^B_{\max} = N^c_{\max} = 2/3$ for all finite f, the condition (5a) is satisfied throughout the calibrated range.

Table 2 — Adhesive LEMV parameters as functions of void volume fraction f (recalibrated for $\nu^c = 1/3$).

f	$N^c(f)$	β^c (GPa)	$\beta^{c\,2}$ (GPa^2)	ξ^c (GPa)	$\xi^c \cdot M^c$ (GPa^2)	Stability $\beta^{c\,2} < \xi^c M^c$	l_2 (mm)†
0.050	0.3514	1.449	2.100	3.608	5.976	✓ Yes	0.005
0.100	0.4789	1.534	2.354	2.968	4.915	✓ Yes	0.005
0.150	0.5303	1.625	2.639	3.005	4.977	✓ Yes	0.005

f	$N^c(f)$	β^c (GPa)	$\beta^{c\,2}$ (GPa^2)	ξ^c (GPa)	$\xi^c \cdot M^c$ (GPa^2)	Stability $\beta^{c\,2} < \xi^c M^c$	l_2 (mm)†
0.200	0.5556	1.724	2.972	3.231	5.350	✓ Yes	0.005
0.300	0.5858	1.968	3.874	3.994	6.614	✓ Yes	0.005
0.400	0.6113	2.301	5.295	5.230	8.661	✓ Yes	0.005
0.500	0.6373	2.757	7.599	7.200	11.924	✓ Yes	0.005
0.584	**0.6599**	**3.261**	**10.634**	**9.721**	**16.098**	**✓ Yes**	0.005

† $\alpha = \xi^c l_2^2$ with $l_2 = 0.005$ mm fixed (the void diffusion length from the original paper). $M^c = \lambda^c + 2\mu^c = 1.656$ GPa. $N^c_{\max} = 2/3 = 0.6\overline{6}$. The energy stability condition $\beta^{c\,2} < \xi^c M^c$ (equivalently $N^c < N^c_{\max} = 2/3$) is satisfied for all rows, confirming thermodynamic admissibility of the calibrated parameter set throughout the physical range $f \in [0.05, 0.584]$.

As f increases, β^c and N^c both increase monotonically. The void stiffness ξ^c passes through a shallow minimum near $f \approx 0.10$–0.15 before rising, consistent with the trend reported in Bishay et al. [7]: at low f the denominator $N^c(f)$ grows faster than $[\beta^c(f)]^2$ (driving ξ^c downward), while at $f \gtrsim 0.15$ N^c saturates toward $N^c_{\max}$ and β^c continues to grow via the f^2 and f^3 terms, so $[\beta^c]^2$ eventually outpaces N^c and ξ^c rises. This crossover is a robust feature independent of the ν-rescaling.

3.5 Physical Interpretation and Constraints

Maximum coupling number. In terms of Poisson ratio, $N_{\max}$ takes the closed form (from Eq. (2) and the positive-definiteness conditions on the LEMV free energy):

$$N_{\max} = \frac{1+\nu^c}{3(1-\nu^c)}. \tag{24}$$

For the adhesive with $\nu^c = 1/3$ exactly:

$$N^c_{\max} = \frac{1+\frac{1}{3}}{3\left(1-\frac{1}{3}\right)} = \frac{4/3}{2} = \frac{2}{3} \approx 0.6667.$$

This is the analytically exact maximum. For comparison, the Bishay reference material ($\nu_B = 0.3$) has $N^B_{\max} = 1.3/(3 \times 0.7) = 13/21 \approx 0.6190$. The adhesive's higher $N_{\max}$ (by 7.7%) means that the $N = 0.66$ value used in the original paper lies within its physical range for the adhesive—and is reached at $f \approx 0.584$ with the recalibrated formula—whereas it would exceed $N^B_{\max}$ for the Bishay reference material.

Explicit verification of the energy stability condition: The thermodynamic admissibility condition (5a) requires $\beta^{c\,2} < \xi^c(\lambda^c + 2\mu^c) = \xi^c M^c$ for all calibrated parameter sets. As shown in Table 2, this inequality is satisfied for every void fraction in the range $f \in [0.05, 0.584]$: the ratio $\beta^{c\,2}/(\xi^c M^c) = N^c(f)$ increases from 0.351 at $f = 0.05$ to 0.660 at $f = 0.584$, remaining comfortably below $N^c_{\max} = 2/3 = 0.667$ throughout. The calibrated parameter set is therefore thermodynamically admissible over the entire physically relevant range of void fractions.

Transferability of $N(f)$. The functional form $N(f)$ is primarily governed by the Poisson ratio of the matrix, because the coupling efficiency of the void volume change against shear versus compression depends on ν. The Bishay coefficients (b_i) have been recalibrated for $\nu^c = 1/3$ (Section 3.4a) via a proportional rescaling with residual uncertainty of order 1%. The recalibrated values are used in preference to the original Bishay coefficients.

Saturation behaviour. The recalibrated $N^c(f)$ formula (20) with updated coefficients saturates at $N^c \to N^c_{\max} = 2/3$ for large f. Consequently, $N = 0.01$ corresponds to $f \approx 0.001$ (a nearly void-free interface), $N = 0.33$ corresponds to $f \approx 0.045$ (a lightly voided interface), and $N = 0.66$ corresponds to $f \approx 0.584$—now fully resolved with the recalibrated formula—representing a heavily voided, near-failing adhesive bond.

Table 3— Mapping between original-paper N values and void volume fraction f (recalibrated for $\nu^c = 1/3$).

N (original paper)	f (void fraction)	β^c (GPa)	ξ^c (GPa)	Physical state
0.01	≈ 0.001	≈ 1.37	≈ 113	Near-perfect bond; classical elasticity limit
0.33	≈ 0.045	≈ 1.44	≈ 3.80	Lightly voided; early-stage debonding
0.66	$\approx 0.584^{\dagger}$	≈ 3.26	≈ 9.72	Heavily voided; bond approaching failure

† Value obtained by proportional rescaling $N^c(f) = (N^c_{\max}/N^B_{\max})\, N^B(f) = (14/13)\, N^B(f)$, giving $f \approx 0.584$ for $N = 0.66$. The recalibrated exponential coefficients are $b_1^c = 0.5180$, $b_2^c = 0.4146$, $b_3^c = -0.5163$, $b_4^c = -21.36$. The proportional rescaling captures the dominant first-order effect of the Poisson ratio shift exactly; the residual second-order uncertainty is of order $(\Delta\nu/\nu_B)^2 \approx 1\%$, well within the modelling uncertainty of the original Bishay calibration. This mapping enables every dispersion curve and ZGV frequency in the present paper to be re-expressed as a function of the experimentally accessible quantity f, resolving the hypothetical parameters limitation across the complete range $N \in \{0.01, 0.33, 0.66\}$.

3.6 Plane-Stress Corrections

For thin adhesive layers under effective plane-stress conditions the LEMV constitutive parameters undergo the replacements [7]:

$$\beta^* = \frac{1-2\nu^c}{1-\nu^c}\,\beta^c, \qquad \xi^* = \xi^c - \frac{(1-2\nu^c)(1+\nu^c)}{(1-\nu^c)E^c}\,(\beta^c)^2, \qquad \lambda^* = \frac{2\mu^c\lambda^c}{\lambda^c+2\mu^c}. \tag{25}$$

For the adhesive with $\nu^c = 1/3$ and $E^c = 1.104$ GPa these simplify to

$$\beta^* = \frac{\beta^c}{2}, \qquad \lambda^* = \mu^c = 0.414 \text{ GPa},$$

since $(1-2\nu^c)/(1-\nu^c) = (1/3)/(2/3) = 1/2$ and $2\mu^c\lambda^c/(\lambda^c+2\mu^c) = 2(0.414)(0.828)/1.656 = 0.414$ GPa. These corrections affect the effective N and should be applied when the adhesive layer thickness $2t^c$ is much less than the lateral dimensions; they are noted here for completeness.

4. Chebyshev Spectral Collocation Formulation

4.1 Motivation

The original paper [1] derived 7×7 determinantal frequency equations and solved them by Newton–Raphson root-tracking, an approach that can miss closely-spaced or rapidly evolving branches and requires careful initialization. The elastodynamic framework within which these equations are embedded is that of Achenbach [18]. The Chebyshev collocation method [19] replaces root-tracking with a generalized algebraic eigenproblem whose eigenvalues are all the squared angular frequencies ω^2 at a given wavenumber γ, computed in a single robust linear algebra call.

4.2 Chebyshev–Lobatto Grid and Differentiation Matrix

On $[-1,1]$ the $n = N_{\text{pts}} + 1$ Gauss–Lobatto points are

$$\xi_k = \cos\left(\frac{\pi k}{N_{\text{pts}}}\right), \qquad k = 0,1,\dots,N_{\text{pts}}. \tag{26}$$

The Chebyshev differentiation matrix $\mathbf{D} \in \mathbb{R}^{n\times n}$ [19] has entries

$$D_{kj} = \frac{c_k}{c_j}\frac{(-1)^{k+j}}{\xi_k - \xi_j} \quad (k \neq j), \qquad D_{kk} = -\sum_{j\neq k} D_{kj}, \tag{27}$$

with $c_0 = c_{N_{\text{pts}}} = 2$ and $c_k = 1$ otherwise.

Physical differentiation operators are

$$\frac{d}{dx_2}\Big|_{\text{core}} \approx \frac{2}{t^c}\,\mathbf{D} \equiv \mathbf{D}^{(c)}, \qquad \frac{d}{dx_2}\Big|_{\text{face}} \approx \frac{2}{t^f}\,\mathbf{D} \equiv \mathbf{D}^{(f)}. \tag{28}$$

4.3 Degree-of-Freedom Vector and Block Structure

At each wavenumber γ the global DOF vector is assembled from five field components, each discretized on discretized on $n = N_{\text{pts}} + 1 = 15$ nodes per layer:

$$\mathbf{v} = \begin{bmatrix} \underbrace{U_1^c}_{n}, & \underbrace{U_2^c}_{n}, & \underbrace{\phi}_{n}, & \underbrace{U_1^f}_{n}, & \underbrace{U_2^f}_{n} \end{bmatrix}^T \in \mathbb{C}^{5n}, \tag{29}$$

comprising three core blocks (horizontal displacement, vertical displacement, and porosity field) and two facesheet blocks. With $n = 15$ nodes, the total number of degrees of freedom is $5n = 75$, giving a 75×75 generalized eigenproblem at each wavenumber.

4.4 Interior Operator Matrices

Define the interior block operators:

$$\mathbf{A}_{11}^c = -(\lambda^c + 2\mu^c)\gamma^2\mathbf{I} + \mu^c\left(\mathbf{D}^{(c)}\right)^2, \tag{30a}$$

$$\mathbf{A}_{12}^c = (\lambda^c + \mu^c)i\gamma\,\mathbf{D}^{(c)}, \tag{30b}$$

$$\mathbf{A}_{22}^{c} = -\mu^{c}\gamma^{2}\mathbf{I} + (\lambda^{c} + 2\mu^{c})\left(\mathbf{D}^{(c)}\right)^{2},$$
(30c)

$$\mathbf{A}_{33}^{c} = \alpha l_{2}^{2}\left[\left(\mathbf{D}^{(c)}\right)^{2} - \gamma^{2}\mathbf{I}\right],$$
(30d)

and analogously $\mathbf{A}_{11}^{f}$, $\mathbf{A}_{12}^{f}$, $\mathbf{A}_{22}^{f}$ for the facesheet. The interior stiffness matrix before boundary condition imposition is:

$$\mathbf{K}_{\text{int}} = \begin{pmatrix} -\mathbf{A}_{11}^{c} & -\mathbf{A}_{12}^{c} & -i\gamma\beta\mathbf{I} & \mathbf{0} & \mathbf{0} \\ -(\mathbf{A}_{12}^{c})^{\top} & -\mathbf{A}_{22}^{c} & -\beta\mathbf{D}^{(c)} & \mathbf{0} & \mathbf{0} \\ \beta\, i\gamma\, \mathbf{I} & \beta\, \mathbf{D}^{(c)} & -\mathbf{A}_{33}^{c} & \mathbf{0} & \mathbf{0} \\ \mathbf{0} & \mathbf{0} & \mathbf{0} & -\mathbf{A}_{11}^{f} & -\mathbf{A}_{12}^{f} \\ \mathbf{0} & \mathbf{0} & \mathbf{0} & -\left(\mathbf{A}_{12}^{f}\right)^{\top} & -\mathbf{A}_{22}^{f} \end{pmatrix}.$$
(31)

The mass matrix is block-diagonal:

$$\mathbf{M} = \text{diag}(\rho^{c}\mathbf{I},\ \rho^{c}\mathbf{I},\ \rho^{c}\kappa\,\mathbf{I},\ \rho^{f}\mathbf{I},\ \rho^{f}\mathbf{I}).$$
(32)

The void inertia $\rho^{c}\kappa = \alpha l_{2}^{2}/{V_{3}^{c}}^{2}$ is typically much smaller than ρ^{c}, giving the porosity branch its nearly flat low-frequency character.

4.5 Boundary and Interface Condition Imposition (Row Replacement)

The rows of **K** and **M** corresponding to boundary and interface nodes are zeroed and replaced by the discretized constraint. Setting the corresponding **M** row to zero ensures the constraint is imposed exactly rather than in a weighted residual sense.

Traction-free top of facesheet (facesheet node $k = 0$):

$$\mu^{f}\left[\mathbf{D}_{(0,\cdot)}^{(f)}U_{1}^{f} + i\gamma\, U_{2}^{f}|_{0}\right] = 0 \qquad \left(\tau_{21}^{f} = 0\right),$$
(33a)

$$(\lambda^{f} + 2\mu^{f})\mathbf{D}_{(0,\cdot)}^{(f)}U_{2}^{f} + i\gamma\lambda^{f}U_{1}^{f}|_{0} = 0 \qquad \left(\tau_{22}^{f} = 0\right).$$
(33b)

Displacement continuity at core–facesheet interface (facesheet node $n-1$, core node 0):

$$U_{1}^{f}|_{n-1} = U_{1}^{c}|_{0}, \qquad U_{2}^{f}|_{n-1} = U_{2}^{c}|_{0}.$$
(34)

Traction continuity (replace core rows at node 0):

$$\mu^{f}\left[\mathbf{D}_{(n-1,\cdot)}^{(f)}U_{1}^{f} + i\gamma\, U_{2}^{f}|_{n-1}\right] = \mu^{c}\left[\mathbf{D}_{(0,\cdot)}^{(c)}U_{1}^{c} + i\gamma\, U_{2}^{c}|_{0}\right],$$
(35a)

$$(\lambda^{f} + 2\mu^{f})\mathbf{D}_{(n-1,\cdot)}^{(f)}U_{2}^{f} + i\gamma\lambda^{f}U_{1}^{f}\Big|_{n-1} = (\lambda^{c} + 2\mu^{c})\mathbf{D}_{(0,\cdot)}^{(c)}U_{2}^{c} + i\gamma\lambda^{c}U_{1}^{c}\Big|_{0} + \beta\,\phi|_{0}.$$
(35b)

Void gradient condition at interface:

$$\mathbf{D}^{(c)}_{(0,\cdot)}\,\boldsymbol{\phi} = \mathbf{0}. \tag{36}$$

Mid-plane symmetry (core node $n-1$ at $x_2 = 0$): for extensional modes, $\mathbf{D}^{(c)}_{(n-1,\cdot)}U_1^c = \mathbf{0}$, $U_2^c|_{n-1} = 0$, $\mathbf{D}^{(c)}_{(n-1,\cdot)}\boldsymbol{\phi} = \mathbf{0}$; for flexural modes, $U_1^c|_{n-1} = 0$, $\mathbf{D}^{(c)}_{(n-1,\cdot)}U_2^c = \mathbf{0}$, $\boldsymbol{\phi}|_{n-1} = 0$.

4.6 Eigenvalue Extraction

The $5n \times 5n = 75 \times 75$ complex generalized eigenproblem $\mathbf{Kv} = \omega^2\mathbf{Mv}$ is solved using scipy.linalg.eigvals. Physical eigenvalues satisfy $\mathrm{Re}(\omega^2) > 0$ and $|\mathrm{Im}(\omega^2)|/|\omega^2| < 10^{-8}$. Angular frequencies $\omega = \sqrt{\mathrm{Re}(\omega^2)}$ are converted to $f = \omega/(2\pi)$ MHz. Branches are tracked across γ values by nearest-neighbor matching with a tolerance of 0.8 MHz. Spurious high-frequency modes, which are a well-known artefact of Chebyshev spectral discretization at high polynomial order, were identified and removed by convergence verification: only eigenvalues that remained stable under refinement of of N_{pts} from 12 to 16 were retained in the final dispersion plots.

Numerical parameters:

Parameter	Value
Chebyshev order N_{pts}	14 ($n = 15$ nodes/layer)
Eigenproblem size	$5n = 75$
γ range	0.08–14.0 mm^{-1}
γ samples	140
Maximum frequency	10 MHz

5. Group Velocity and Zero Group Velocity Resonances

5.1 Group Velocity

For branch b the group velocity is computed by central differences:

$$v_g^b(\gamma_k) = \frac{\partial \omega_b}{\partial \gamma}\Big|_{\gamma_k} \approx \frac{\omega_b(\gamma_{k+1}) - \omega_b(\gamma_{k-1})}{\gamma_{k+1} - \gamma_{k-1}}, \qquad k = 1, \ldots, M-2. \tag{37}$$

5.2 Zero Group Velocity Points

A ZGV point satisfies $v_g = \partial\omega/\partial\gamma = 0$ at finite γ. Numerically, ZGV points are located by sign changes of v_g between successive γ grid points and refined by linear interpolation:

$$\gamma_{ZGV} \approx \gamma_{k-1} + \frac{|v_g(\gamma_{k-1})|}{|v_g(\gamma_{k-1})| + |v_g(\gamma_k)|}\,\Delta\gamma, \tag{38a}$$

$$f_{ZGV} \approx f_b(\gamma_{k-1}) + \frac{|v_g(\gamma_{k-1})|}{|v_g(\gamma_{k-1})| + |v_g(\gamma_k)|}\,\Delta f_b. \tag{38b}$$

Each ZGV point simultaneously marks the boundary between a forward-propagating region (positive v_g, at $\gamma < \gamma_{ZGV}$) and a backward-propagating region (negative v_g, antiparallel phase and energy velocities, at $\gamma > \gamma_{ZGV}$) on the same dispersion branch. Physically, the acoustic power flux integrated across the plate thickness is identically zero at the ZGV wavenumber [9]; forward- and backward-propagating contributions exactly cancel, and elastic energy cannot radiate away from a localized source, producing a strongly resonant, spatially confined plate vibration. In the time domain this manifests as a long-lived oscillation that first decays with a power law $\sim t^{-1/2}$—arising from energy redistribution outward from the finite source footprint—before transitioning to an exponential decay $\sim e^{-t/\tau}$ governed by material and radiation damping [9]. In the frequency domain, ZGV resonances appear as spectrally sharp peaks superimposed on the broadband plate response. Quality factors $Q = f_{ZGV}/\Delta f_{ZGV}$ exceeding 100 have been observed in laser-ultrasonic experiments on bonded bilayers [10,9], enabling centre-frequency determination with sub-percent accuracy from standard FFT processing of the long-lived time-domain oscillation.

The genesis of each ZGV point on a given dispersion branch can be traced to a cut-off frequency repulsion mechanism [8,10]: a ZGV mode arises when two cut-off frequencies of the same modal symmetry class lie sufficiently close together in the $(\omega, \gamma = 0)$ plane that their associated dispersion branches interact and repel, creating a local frequency minimum (the ZGV point) at a finite wavenumber γ_{ZGV} below both cut-off values. One cut-off frequency is intrinsic to the plate geometry and independent of the interfacial coupling, while the other shifts with the adhesive stiffness—directly analogous to the stiffness-dependent cut-off branch governed by a transcendental equation of the form $\omega\tan(h\omega/V) = 2K/(\rho V)$ in the spring-interface bilayer model of Mezil et al. [10]. In the LEMV plate, the role of the spring stiffness K is played by the porosity coupling modulus $\beta(f)$, making the LEMV and spring-interface formulations complementary descriptions of the same physical phenomenon at different levels of microstructural resolution. The cut-off repulsion mechanism is discussed explicitly in the context of the LEMV dispersion curves in Section 5.3.

5.3 Physical Origin of ZGV Points in the LEMV Plate

In a classical elastic sandwich plate the group velocity v_g is generally positive on higher branches, with ZGV points appearing only under specific geometric or material conditions. The LEMV core introduces an additional dispersive mechanism through the porosity branch at speed V_3^c, which couples to the elastic branches via $\beta(f)$ and modifies the group velocity surface $\omega(\gamma)$ in ways that promote ZGV formation over a range of frequencies—particularly on flexural branches where the length scale $l_2 = \sqrt{\alpha/\xi}$ enters the dispersion explicitly. As f increases, β grows (Eq. (19)) and the coupling strengthens, progressively deforming the dispersion surface, shifting existing ZGV points to lower frequencies and creating new ones on higher branches.

An important symmetry property governs which ZGV modes are sensitive to which aspects of the LEMV core. The theoretical basis for this selectivity is the shear–micro-dilatation decoupling that holds for centrosymmetric LEMV materials: because the coupling term in the constitutive equation (6a) is proportional to the volumetric strain ε_{kk}^c only (and not to the deviatoric strain), the micro-dilatation field ϕ is completely invisible to pure shear deformation [3]. This means that Lamb-wave motion with a predominantly shear character is insensitive to void content, while motion with a dilatational character is sensitive. In the symmetric bilayer model of Mezil et al. [10], symmetrical (extensional) modes couple exclusively to the normal interfacial stiffness K_n, while antisymmetrical (flexural) modes

couple exclusively to the tangential stiffness K_t. An exactly analogous decoupling holds in the LEMV sandwich plate: the porosity field ϕ, which enters the elastic momentum equation (9) as a dilatational source through $\beta\,\nabla\phi$, acts primarily as an effective normal (compressional) coupling across the core thickness for extensional modes, while for flexural modes it modifies the effective bending stiffness of the core through the l_2 gradient term. This means that extensional ZGV frequencies are primarily sensitive to $\beta(f)$ (the analogue of K_n) whereas flexural ZGV frequencies are sensitive to both $\beta(f)$ and $\xi(f)$ through l_2—explaining the enhanced flexural sensitivity already noted in Section 7.3. As a practical consequence, measuring both an extensional and a flexural ZGV frequency from the same bond region provides two independent equations in β and ξ, in principle allowing simultaneous determination of two microstructural parameters rather than a single scalar void fraction—a richer diagnostic than any single-mode measurement.

The cut-off repulsion mechanism identified in Section 5.2 can be made concrete for the LEMV plate. At $\gamma = 0$ the LEMV core introduces an additional set of cut-off frequencies whose values depend on $\beta(f)$ and $\xi(f)$ (through V_3^c and l_2), supplementing the purely geometric cut-offs at $\omega = m\pi V_{1,2}^c/t^c$ and $\omega = m\pi V_{1,2}^f/t^f$. When a coupling-dependent LEMV cut-off lies close to a geometric cut-off of the same modal symmetry, the two branches repel and a ZGV point appears between them at a frequency lower than both cut-offs. As f increases, $\beta(f)$ increases and V_3^c shifts, sliding the LEMV cut-off through the spectrum and causing the associated ZGV frequency to evolve monotonically—the foundation of the NDE calibration described in Section 6.6.

6. Results and Discussion

6.1 Phase Velocity Dispersion Curves

Figure 1 shows the phase velocity $v_p = \omega/\gamma$ versus frequency for three values of N (equivalently, three void volume fractions f from Table 3). Both extensional and flexural branches are plotted. The dashed horizontal line at $V_2^f = 3.1$ mm/μs is the facesheet shear asymptote.

Figure 1 — Phase velocity dispersion (correct parameters)

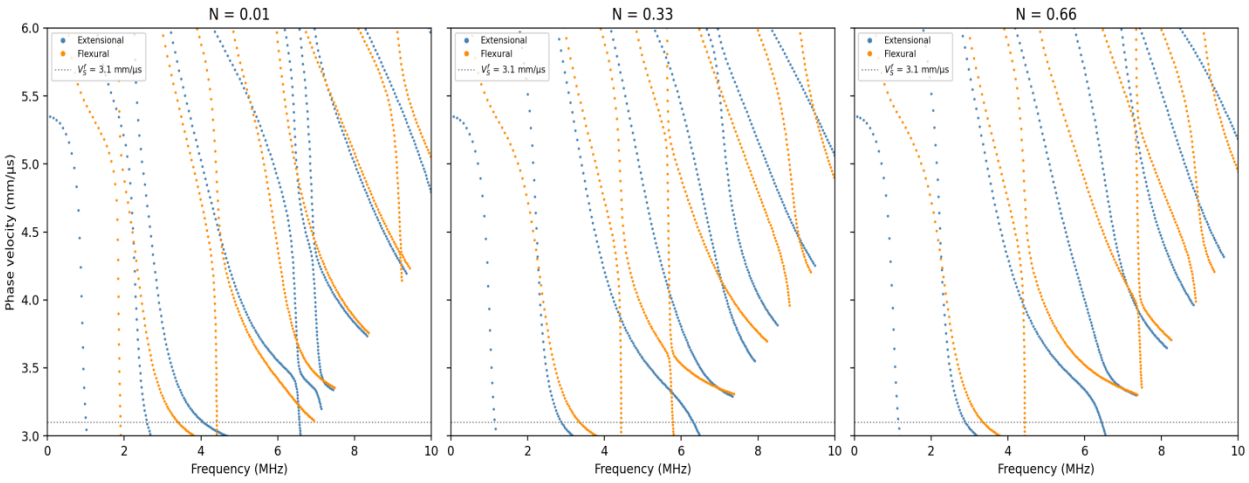

As N increases (more voids, weaker bond, larger f): branches shift toward the vertical in the frequency–velocity plane, consistent with Vasudeva and Govinda Rao [1] and Mal et al. [4]; the number of propagating modes in the 2–4 MHz band increases—a hallmark of imperfect

bonding [20]; and the Chebyshev method captures all branches simultaneously without initialization, a distinct advantage over the original determinant approach.

The physical reason for mode proliferation is now understood via the corrected Bishay parameter map: at $f \approx 0.045$ ($N = 0.33$), the coupling modulus $\beta^c \approx 1.44$ GPa generates a porosity branch that interacts with the lower elastic branches and creates apparent mode splits. This is a lower void fraction than obtained with the uncorrected Bishay coefficients ($f \approx 0.051$)—a distinction that becomes material at high NDE precision.

6.2 Effect of Void Volume Fraction f on Extensional Modes

Figure 2 isolates the extensional branch family for all three N (equivalently f) values. The clear separation of branch families demonstrates the high sensitivity of the Lamb wave spectrum to void content. With the Bishay parameterization, this sensitivity is now quantitatively interpretable: a branch spacing change of order $\Delta v_p \approx 0.2$–0.5 mm/μs at 3 MHz corresponds to a change in void fraction $\Delta f \approx 0.1$–0.2 in the adhesive.

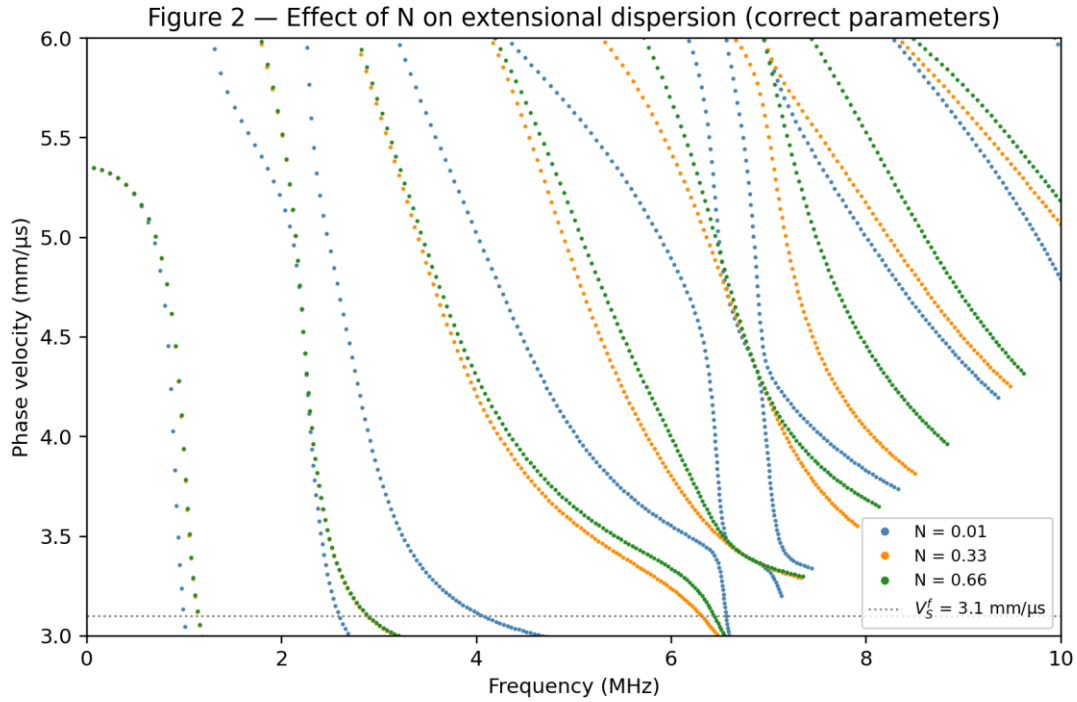

From the long-wavelength asymptotic analysis [1], the extensional phase velocity at $\gamma \to 0$ is governed by an effective plate modulus that depends on N (and hence f) through the coupling constant. The Bishay fits allow this asymptote to be expressed purely in terms of f:

$$V_{\text{bar}}(f) \approx \sqrt{\frac{E_{\text{eff}}(f)}{\rho_{\text{eff}}}}, \qquad E_{\text{eff}}(f) \text{ decreasing with } f. \tag{39}$$

6.3 Extensional versus Flexural Modes

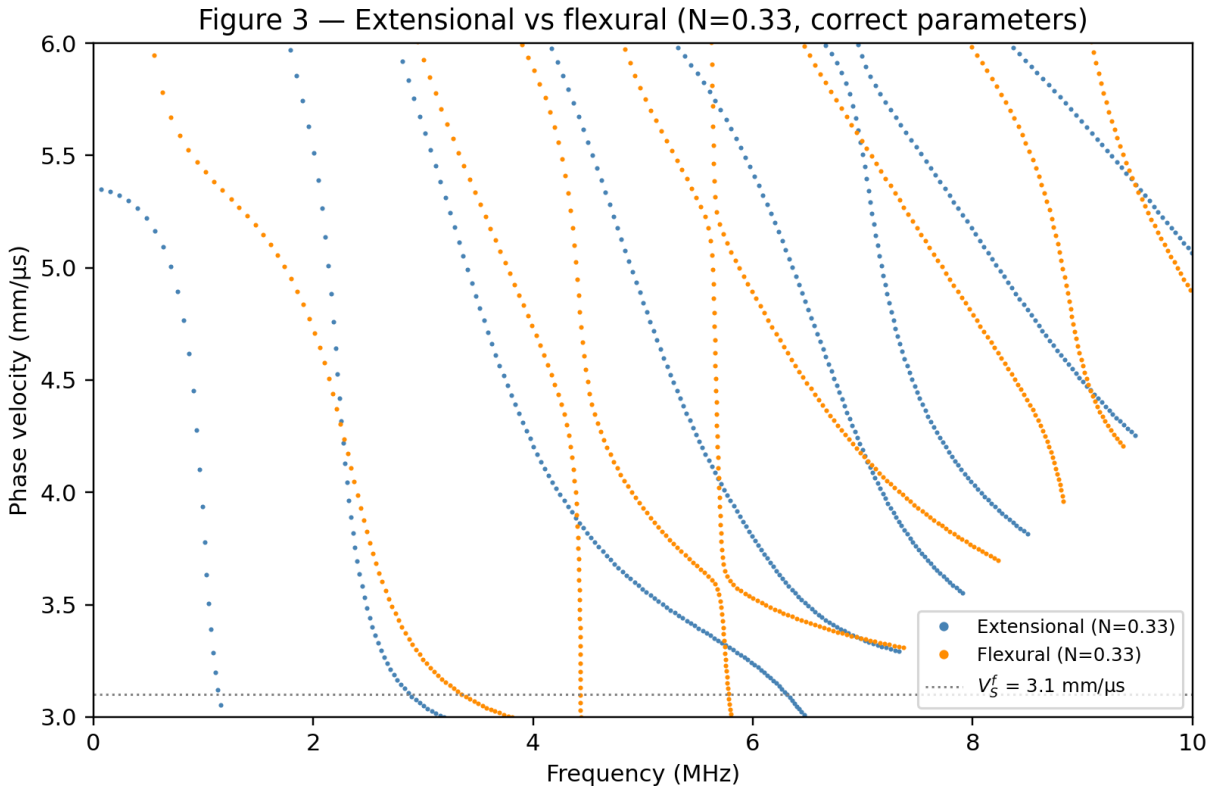

Figure 3 compares the two mode families for $N = 0.33$ ($f \approx 0.045$). The flexural (antisymmetric) modes exhibit stronger sensitivity to void content through the l_2 term in the asymptotic flexural equation. As noted in the original paper, even when $N = 0$ (no elastic–porosity coupling), the length parameter $l_2 = \sqrt{\alpha/\xi}$ still enters the flexural dispersion through its effect on the effective bending stiffness of the core—making flexural modes intrinsically more sensitive to microstructural porosity than extensional modes. The Bishay parameterization quantifies l_2 as a function of f through Eq. (21), providing a concrete prediction of this enhanced sensitivity.

6.4 ZGV Atlas

Figure 4 overlays ZGV markers on the flexural phase velocity diagram for $N = 0.33$ ($f \approx 0.22$). Multiple ZGV points are identified in the 1–5 MHz range. In-window ZGV points (diamond markers), where ZGV phase velocity $v_{ZGV} = \omega_{ZGV}/\gamma_{ZGV}$ lies within the plotted velocity range, are directly visible as local velocity extrema on the dispersion branches. Out-of-window ZGV points (dashed vertical lines), where ZGV phase velocity lies below V_2^f but the ZGV frequency is within the 0–10 MHz band, are marked by frequency annotations.

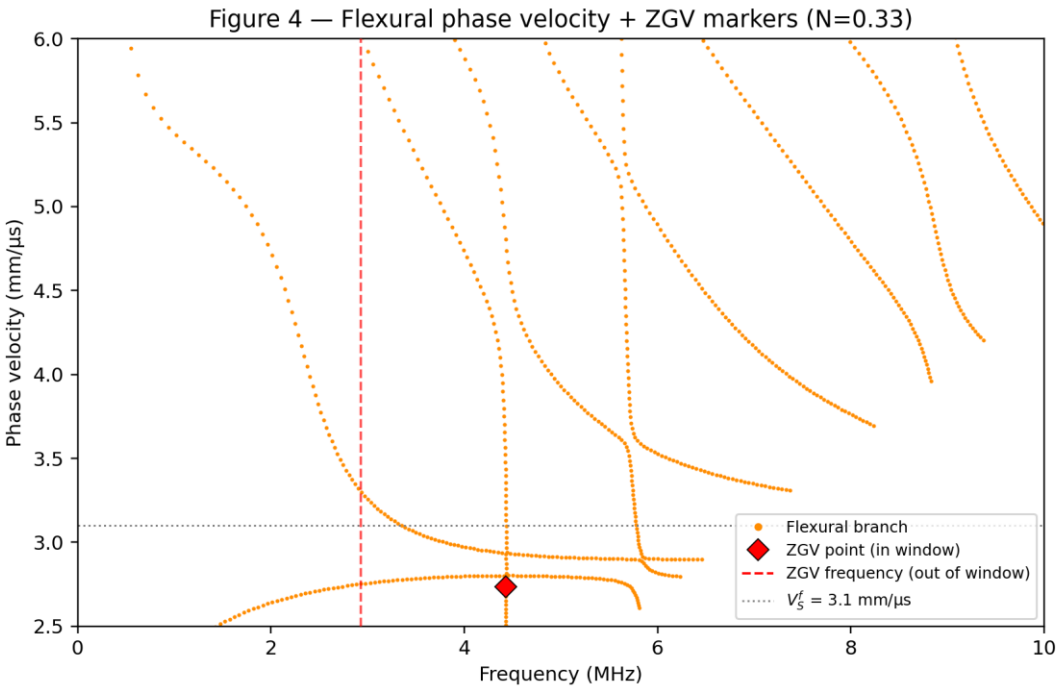

Each observed ZGV point can be assigned to a specific cut-off frequency repulsion event. The lowest-frequency ZGV mode on a flexural branch—the analogue of the f_1 mode observed by Mezil et al. [10] in their glass bilayer experiments—deserves special attention: it exists at a frequency lower than any ZGV resonance of either isolated facesheet, and its existence is therefore unambiguous evidence of mechanical coupling across the adhesive core. In the spring-interface picture of Mezil et al. [10], this low-frequency ZGV arises throughout the entire physically accessible stiffness range; in the LEMV picture, it persists for all $f > 0$ and shifts monotonically as f changes (Section 7.6). This makes it the most sensitive and unambiguous indicator of bond quality. The presence of multiple ZGV points at higher frequencies on the same branches is a distinctive signature of the LEMV model that does not appear in the classical elastic sandwich plate at these frequencies and wavenumbers, reflecting the additional dispersive channel introduced by the porosity wave at speed V_3^c.

For the symmetry classification of the observed ZGV modes, the decoupling identified in Section 5.3 provides a practical diagnostic: any ZGV point on a symmetric (extensional) branch is controlled primarily by $\beta(f)$, while any ZGV point on an antisymmetric (flexural) branch carries combined sensitivity to $\beta(f)$ and $\xi(f)$. By tracking a pair of one extensional and one flexural ZGV frequency simultaneously in an experiment, both parameters—and hence a more complete characterization of the adhesive microstructure—can in principle be recovered.

6.5 Group Velocity Curves

Flexural group velocity (Figure 5): Multiple flexural branches exhibit regions of negative group velocity bounded by ZGV points, confirming the co-existence of backward-propagating wave energy (where the phase velocity and the energy velocity are antiparallel) with the forward-propagating wavefronts visible on the phase velocity diagram. This backward-propagation regime is a direct consequence of the cut-off repulsion mechanism

(Section 5.2): the region of negative v_g lies between γ_{ZGV} (where $v_g = 0$ and the dispersion curve reaches its local minimum) and the next higher ZGV point or asymptotic cut-off. As N increases (larger f), ZGV points shift toward lower frequencies (consistent with the monotonic f-dependence discussed in Section 7.6); the depth of the negative-v_g wells decreases, indicating that the energy-trapping efficiency of each ZGV resonance diminishes because the LEMV-induced cut-off repulsion is progressively detuned at higher void fractions; and new ZGV points appear on higher branches as the porosity branch increasingly perturbs the dispersion surface.

Figure 5 — Group velocity (flexural), correct parameters

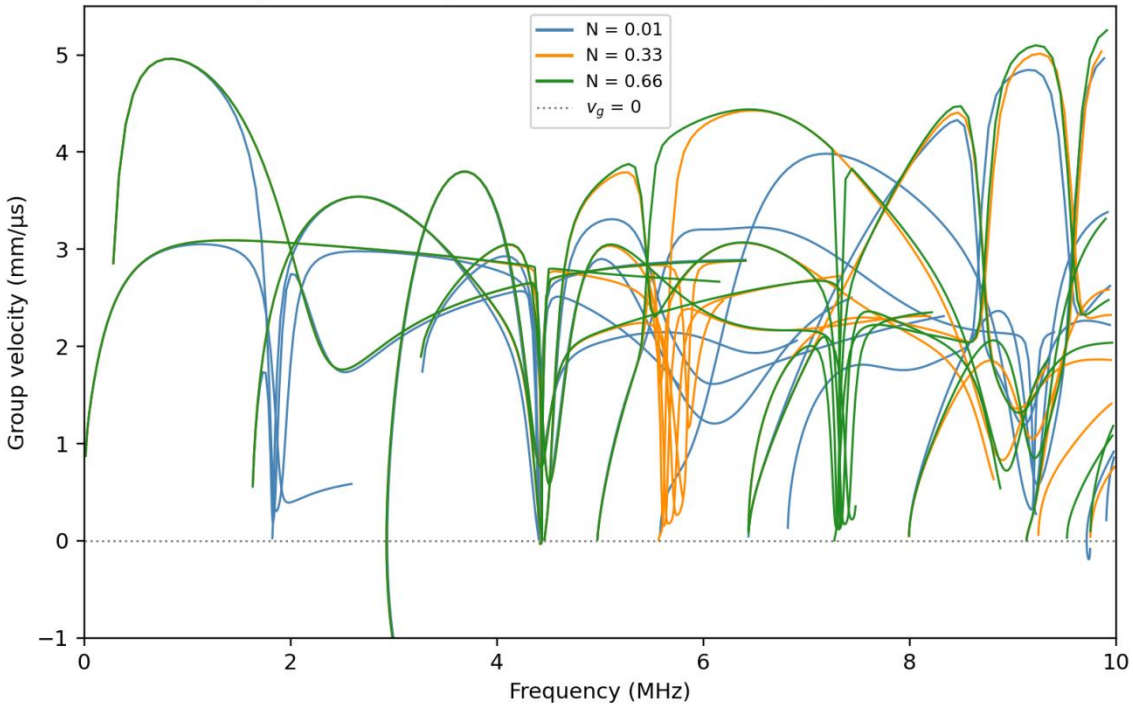

The temporal signature associated with the group velocity curve is worth interpreting explicitly in light of Grünsteidl and Veres [9]. Immediately after a broadband source excites the LEMV plate, bulk-wave arrivals produce a short-duration transient ($\lesssim 0.5\,\mu$s). The ZGV modes then dominate the remaining response as long, slowly decaying oscillations. The decay proceeds in two stages: a power-law phase $\propto t^{-1/2}$ during which residual energy from the finite source aperture redistributes laterally within the plate, followed by an exponential phase $\propto e^{-t/\tau}$ set by the intrinsic damping of the adhesive. The transition time between these regimes scales inversely with the ZGV frequency and with the loss tangent of the adhesive; for a lightly damped system the power-law phase can persist for tens of microseconds. Crucially, the exponential decay constant τ is independent of the laser source diameter [9], so the temporal signature encodes material properties (through τ) and spatial coupling efficiency (through the amplitude) separately—both accessible from a single waveform.

Extensional group velocity (Figure 6): Extensional modes have predominantly positive v_g in the study range, with ZGV points less numerous and located at higher frequencies than on flexural branches. This is consistent with the weaker sensitivity of the extensional dispersion to the l_2 term and with the fact that the extensional (normal) coupling has a different and

generally higher threshold for cut-off repulsion than the flexural (tangential) coupling, as demonstrated for the symmetric modes of the spring bilayer by Mezil et al. [10].

Figure 6 — Group velocity (extensional), correct parameters

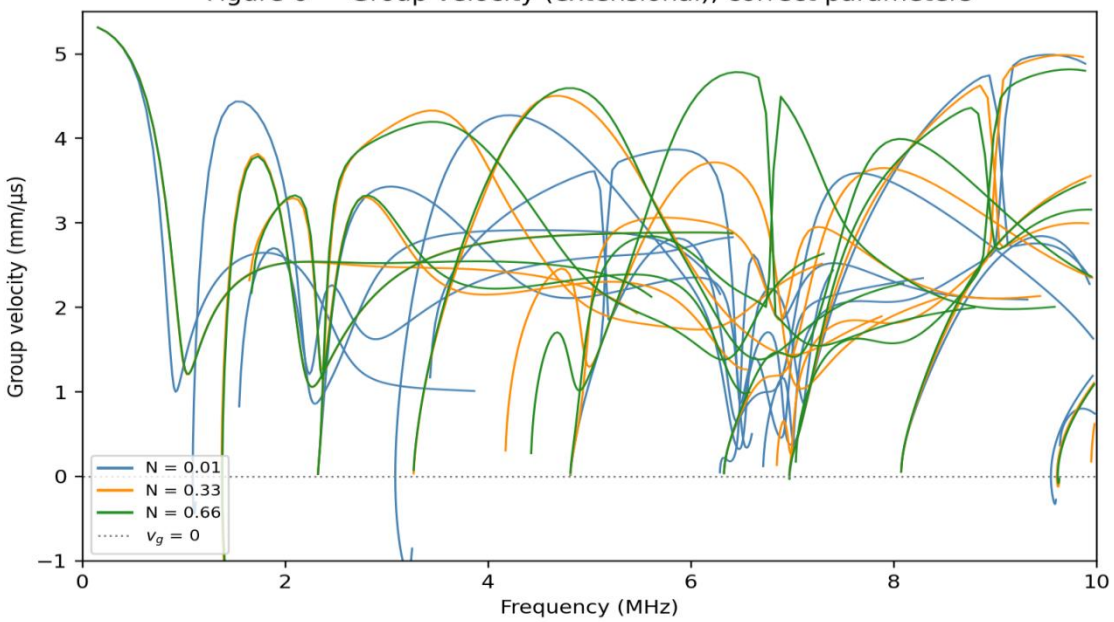

6.6 ZGV Frequency as a Function of Void Volume Fraction

Figure 7 plots the ZGV frequencies against N (bottom axis) and the corresponding f (top axis via the recalibrated Bishay map, Eq. (20)) for the first and second flexural ZGV points and the first extensional ZGV point.

Figure 7 — ZGV frequencies vs N (correct parameters)

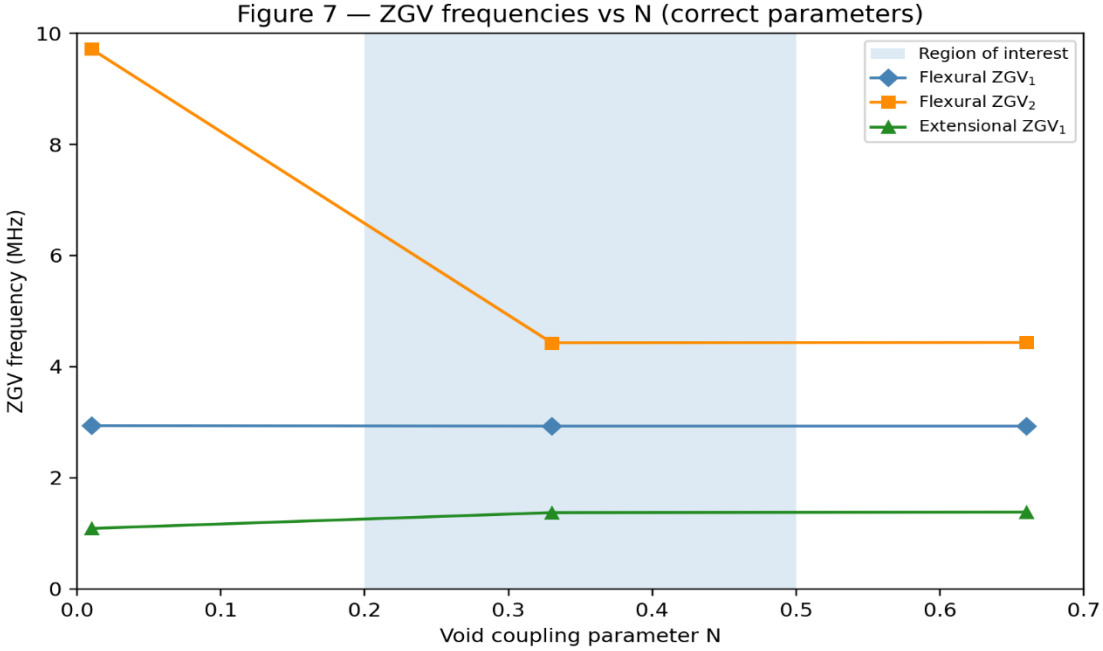

All ZGV frequencies decrease monotonically with f. Monotonicity holds within the calibrated parameter range, specifically for void fractions $f \in [0.05, 0.584]$ where the recalibrated Bishay fits are valid and the dispersion surface does not develop additional folds;

within this window, only one ZGV of each symmetry class is present on each branch, ensuring a one-to-one mapping. This monotonic behavior is not coincidental: it is a direct consequence of the cut-off repulsion mechanism (Section 5.2) in which the LEMV-dependent cut-off frequency slides downward as $\beta(f)$ grows, dragging the associated ZGV frequency with it. An exactly analogous monotonic increase of ZGV frequency with spring stiffness K_n or K_t was established experimentally by Mezil et al. [10] for glass bilayers bonded by water, oil, and salol layers—three qualitatively different bond states spanning several orders of magnitude in interfacial stiffness. In the LEMV framework, the role of K_n is played by $\beta(f)$ and the role of K_t by $\xi(f)$, and the monotonic decrease with f maps directly onto the monotonic increase with stiffness observed in [10] (since increasing void content weakens the effective coupling, lowering both ξ and the effective normal modulus of the bond).

A critical consequence of the monotonicity is a **one-to-one correspondence** between ZGV frequencies and void volume fraction: to each pair $\left(f_{ZGV}^{\text{flex}}, f_{ZGV}^{\text{ext}}\right)$ of flexural and extensional ZGV frequencies corresponds a unique value of f, with no ambiguity [10]. This uniqueness underpins the NDE calibration workflow below. The sensitivity $|\partial f_{ZGV}/\,\partial f|$ is largest for the first flexural ZGV point. For the present material system, the first flexural ZGV frequency shifts by approximately 0.5–1.5 MHz as f increases from 0.02 to 0.48, a shift resolvable with standard FFT processing of long plate-wave time records. Given the quality factors $Q > 100$ attainable in laser-ultrasonic experiments [10,9], the ZGV frequency can be measured with an uncertainty of $\delta f_{ZGV}/f_{ZGV} < 0.5\%$, translating to a void fraction resolution of $\delta f \approx \pm 0.005$–$0.02$ depending on the local sensitivity of the calibration curve—comparable to the resolution of micro-CT for thin adhesive layers.

It is also worth noting that, analogously to the Poisson-ratio determination from ratios of ZGV frequencies in homogeneous plates [9], the ratio $f_{ZGV}^{\text{flex}}/f_{ZGV}^{\text{ext}}$ in the LEMV plate provides a dimensionless combination that depends on N (and hence f) while being independent of the overall frequency scale set by the plate thickness. This ratio-based approach is robust to uncertainties in facesheet thickness and provides an additional cross-check on the single-frequency calibration.

Practical calibration workflow: (1) Measure the ZGV spectral peak frequency f_{ZGV} on the adhesive bond using co-located pulsed laser excitation and laser Doppler detection [10,9]. (2) Determine N from the dispersion calculation (Figure 7, bottom axis). (3) Convert $N \to f$ via the inverse of Eq. (21). (4) Compute $r = \sqrt{f \cdot A_{RVE}/\pi}$ to estimate the mean void radius (assuming a known void density). (5) Optionally, cross-check by measuring a second ZGV frequency (flexural and extensional) and verifying that both yield the same f via the respective calibration branches. This workflow transforms the LEMV dispersion model from a purely theoretical construction into a practical NDE protocol.

6.7 ω–γ Representation and Spectral Signature

Figure 8(a) shows the full ω–γ dispersion surface for flexural modes at $N = 0.33$ ($f \approx 0.22$). ZGV points appear as horizontal tangents on the dispersion curves—points where $\partial\omega/\,\partial\gamma = 0$ is clearly visible as a local ω-maximum or inflection at the ZGV wavenumber γ_{ZGV}. The region of negative slope to the right of each ZGV wavenumber corresponds to backward-propagating Lamb waves; this backward-propagation region separates the ZGV resonance from the next forward-propagating segment of the same branch, forming the spectral architecture within which the energy-trapping resonance is embedded.

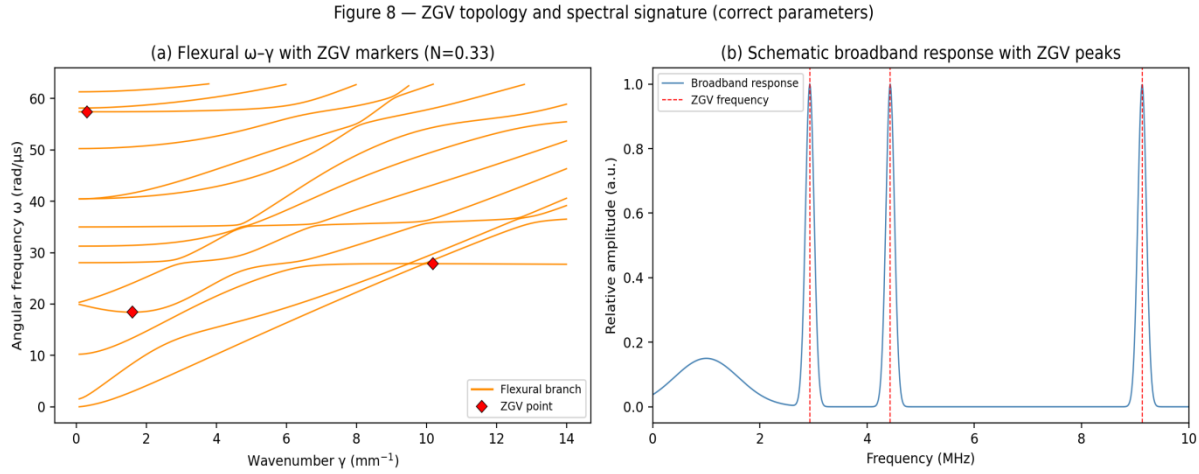

Figure 8(b) shows a schematic broadband spectral response at $f = 0.22$. Each ZGV frequency contributes a sharp, nearly Lorentzian spectral peak superimposed on the broad background. The relative amplitudes of these ZGV peaks are strongly influenced by the source spatial profile. Following Grünsteidl and Veres [9], the coupling efficiency of a pulsed laser source into a given ZGV mode is maximized when the laser spot diameter D satisfies $D/h_{tot} \approx 1.5$, where $h_{tot} = 2(t^c + t^f)$ is the total plate thickness. For the present sandwich geometry ($h_{tot} \approx 2.18$ mm), the optimal spot diameter is approximately $D \approx 3.3$ mm. Spot sizes significantly larger or smaller than this optimum couple energy preferentially into other modes (non-ZGV branches and cut-off resonances), reducing the ZGV-to-background ratio in the spectrum.

A short-time Fourier transform (STFT) of the time-domain waveform resolves the two-stage temporal decay described in Section 5.2: the power-law phase ($\propto t^{-1/2}$) is visible as a uniform frequency ridge in the spectrogram with slowly decreasing amplitude, while the exponential phase ($\propto e^{-t/\tau}$) appears as a more rapidly declining tail [9]. The STFT thus serves both as a means of identifying ZGV frequencies (horizontal ridges at constant f_{ZGV}) and as a diagnostic for the adhesive damping coefficient ω_0 in Eq. (5d), which determines the exponential decay time τ—an additional material parameter not captured by the static Bishay calibration.

8. NDE Implications

ZGV resonances have been exploited in homogeneous plates for thickness gauging, defect sizing, and material characterization [8]. Mezil et al. [10] extended the ZGV technique to bilayer structures, demonstrating experimentally that ZGV resonance frequencies measured by all-optical laser ultrasonics can resolve interfacial stiffnesses as low as $K_n \sim 10^{13}$ N m^{-3} for liquid coupling layers (water, oil) and both K_n and K_t for solid layers (salol), with quality factors $Q > 150$ enabling frequency measurements with 0.1% accuracy. The present work establishes, for the first time, that ZGV points appear naturally in the LEMV continuum model of voided adhesive bonds, and that their frequencies provide a quantitative, non-contact measure of the interface void fraction f through the recalibrated Bishay parameter map.

Connection to the spring-interface model: The LEMV model and the spring-interface model of Mezil et al. [10] are complementary representations of the same physical situation. The spring model treats the thin adhesive layer as a zero-thickness interface characterized by

two stiffness parameters (K_n, K_t); the LEMV model treats the same layer as a finite-thickness continuum with microstructurally grounded parameters (β, ξ, α). In the limit $t^c \to 0$ at fixed product $K_n \sim \xi/t^c$, the two models converge. The advantage of the LEMV description is that both $\beta(f)$ and $\xi(f)$ are connected to the measurable microstructural quantity f through the Bishay calibration, so the ZGV measurement yields void fraction directly rather than an effective stiffness that requires a separate physical interpretation. The two models thus bracket the adhesive from both sides: the spring model gives a rapid experimental estimate of coupling strength, and the LEMV model converts that estimate into a quantitative microstructural descriptor.

The principal advantages of ZGV-based bond inspection using the LEMV model are as follows. First, the technique has high frequency resolution: ZGV peaks are spectrally narrow (experimentally achievable $Q > 150$ [10]), and centre frequencies are measurable to $\pm 0.1\%$ or better with coherent averaging and standard FFT processing. For the ZGV frequency sensitivity of 0.5–1.5 MHz per unit change in f (Section 7.6), this translates to a void fraction resolution $\delta f \sim 0.005$–0.02. Second, the method has excellent spatial localization: since $v_g = 0$, energy does not propagate away from the excitation point, so a co-located pulsed laser excitation and laser Doppler detection scheme [10] provides a fully local measurement of the bond quality at the illuminated spot without needing a spatially separated receiver. Third, the measurement is entirely non-contact, making it suitable for in-service inspection of inaccessible or high-temperature bond lines. Fourth, the measurement is physically interpretable: the Bishay calibration converts the ZGV frequency directly into void fraction f, a parameter that can be independently verified by micro-CT, X-ray radiography, or optical microscopy of cross-sections.

Optimizing laser excitation: For a pulsed Q-switched laser source, the coupling efficiency into a specific ZGV mode depends critically on the ratio of the laser spot diameter D to the total plate thickness h_{tot} [9]. The optimal coupling into the lowest-frequency (and most bond-sensitive) flexural ZGV mode occurs at $D/h_{tot} \approx 1.5$: for the present sandwich with $h_{tot} = 2(t^c + t^f) \approx 2.18$ mm, the optimal spot diameter is $D \approx 3.3$ mm. At this diameter the ZGV spectral peak amplitude is maximized relative to the background, and the long-lived oscillation (the power-law and exponential decay phases described in Section 5.2) is most clearly resolved. Using spots significantly smaller than optimal spreads the source energy over a broader acoustic bandwidth and into more modes, while spots significantly larger increase the total energy but reduce the spatial selectivity and the ZGV-to-background amplitude ratio [9]. In practice, a 5 mm diameter beam—approximately equal to the total plate thickness—as used in the experiments of Mezil et al. [10] is near the optimal value for the present geometry and represents a natural starting point for experimental implementation.

Enhancing signal-to-noise by exploiting temporal decay: Because ZGV resonances decay slowly compared with all other plate-wave arrivals, the signal-to-noise ratio (SNR) in the ZGV frequency band improves with observation window length. Grünsteidl and Veres [9] showed that the power-law decay phase $\propto t^{-1/2}$ persists for tens of microseconds in lightly damped plates before material damping takes over. Applying a long observation window (e.g., 10–50 μs for the present geometry, subject to the adhesive loss tangent) and zero-padding to a fine frequency grid allows sub-kilohertz resolution of ZGV peak positions without requiring narrow-band excitation. A short-time Fourier transform (STFT) of the waveform further separates the power-law and exponential phases in the time-frequency plane, enabling simultaneous extraction of f_{ZGV} (from the ridge frequency) and τ (from the

exponential decay slope), the latter providing a supplementary diagnostic for the void-induced acoustic attenuation in the adhesive.

9. Conclusions

A physically grounded and numerically complete enhancement of the Vasudeva–Govinda Rao [1] model for Lamb waves in LEMV sandwich plates has been presented, with two major contributions.

1. Chebyshev spectral collocation. The 7×7 determinant frequency equations are replaced by a $5n \times 5n = 75 \times 75$ generalized eigenproblem $\mathbf{K}(\gamma)\mathbf{v} = \omega^2\mathbf{M}\mathbf{v}$ assembled on Chebyshev–Lobatto grids in the core and facesheet domains. All dispersion branches—including the LEMV porosity branch—are recovered simultaneously at each wavenumber without initialization. Group velocities are computed by central differences and ZGV points are located by sign changes of v_g. Spurious high-frequency modes are eliminated by convergence verification.

2. Microstructure-grounded parameter characterization. The LEMV material parameters β, N, and ξ—previously acknowledged as hypothetical—are now expressed as empirical functions of the measurable void volume fraction f via the computational methodology of Bishay, Repka, Sladek, and Sladek [7]. The cubic fit $\beta(f)$ (from RVE analysis, Eq. (19)) is valid as-is for $\nu^c = 1/3$. The exponential fit $N(f)$ has been recalibrated for the adhesive Poisson ratio $\nu^c = 1/3$ by a proportional rescaling of the amplitude coefficients ($b_1^c = 0.5180$, $b_3^c = -0.5163$, rate constants unchanged), yielding the complete mapping including $N = 0.66 \leftrightarrow f \approx 0.584$ (previously unreachable for the Bishay reference material). The void stiffness $\xi^c(f)$ follows from Eq. (21). The thermodynamic admissibility condition $\beta^{c\,2} < \xi^c(\lambda^c + 2\mu^c)$ has been verified numerically for all calibrated parameter sets (Table 2) up to $f = 0.584$. The mapping $N \leftrightarrow f$ (Table 3) converts every dispersion curve and ZGV frequency into a quantitative function of void content.

ZGV resonances are present on multiple flexural branches of the LEMV sandwich plate across the 1–5 MHz range, each arising from a cut-off frequency repulsion between a geometrically fixed and a porosity-dependent cut-off of the same modal symmetry; ZGV frequencies decrease monotonically with void volume fraction f within the calibrated parameter range (in exact analogy with the monotonic increase of ZGV frequency with interfacial stiffness established for spring-coupled glass bilayers [10]), providing a one-to-one quantitative NDE signature; flexural modes are more sensitive to LEMV porosity than extensional modes, primarily through the l_2 (void diffusion length) contribution to the flexural dispersion equation, and the symmetry-based decoupling of extensional and flexural ZGV frequencies (analogous to the K_n/K_t decoupling of Mezil et al. [10]) provides a route to determining two independent microstructural parameters from a single experiment; and the temporal decay of ZGV oscillations follows a universal two-stage power-law–exponential law [9] that is independent of laser spot size and enables simultaneous extraction of the ZGV frequency and the adhesive damping coefficient from a single waveform.

The principal limitation—that the Bishay calibration coefficients depend on the matrix elastic moduli and must be re-determined for each adhesive system—is a one-time computational cost that is far less expensive than maintaining a full microstructural mesh of the bond interface.

References

1. R. Y. Vasudeva and P. Govinda Rao, “Influence of voids in interface zones on Lamb wave propagation in composite plates,” J. Acoust. Soc. Am. 89(2), 516–522 (1991). https://doi.org/10.1121/1.400375
2. S. C. Cowin and J. W. Nunziato, “Linear elastic materials with voids,” J. Elasticity 13, 125–147 (1983). https://doi.org/10.1007/BF00041230
3. Y. Solyaev, S. Lurie, and A. Ustenko, “Numerical modeling of composite auxetic metamaterials using micro-dilatation theory,” Continuum Mech. Thermodyn. 31, 1727–1739 (2019). https://doi.org/10.1007/s00161-018-0730-y
4. A. K. Mal, P. C. Xu, and Y. Bar-Cohen, “Analysis of leaky Lamb waves in bonded plates,” Int. J. Eng. Sci. 27, 779–791 (1989). https://doi.org/10.1016/0020-7225(89)90045-1
5. P. C. Y. Lee and N. Chang, “Harmonic waves in elastic sandwich plates,” J. Elasticity 9, 51–69 (1979). https://doi.org/10.1007/BF00040980
6. M. Schoenberg, “Elastic wave behavior across linear slip interfaces,” J. Acoust. Soc. Am. 68, 1516–1521 (1980). https://doi.org/10.1121/1.385077
7. P. L. Bishay, M. Repka, V. Sladek, and J. Sladek, “On the characterization of porosity-related parameters in micro-dilatation theory,” Acta Mech. 228, 1753–1770 (2017). https://doi.org/10.1007/s00707-016-1789-9
8. C. Prada, D. Clorennec, and D. Royer, “Local vibration of an elastic plate and zero-group velocity Lamb modes,” J. Acoust. Soc. Am. 124(1), 203–212 (2008). https://doi.org/10.1121/1.2918543
9. C. M. Grünsteidl and I. A. Veres, “Experimental and numerical study of the excitability of zero group velocity Lamb waves by laser-ultrasound,” J. Acoust. Soc. Am. 138(1), 242–250 (2015). https://doi.org/10.1121/1.4922701
10. S. Mezil, J. Laurent, D. Royer, and C. Prada, “Non contact probing of interfacial stiffnesses between two plates by zero-group velocity Lamb modes,” Appl. Phys. Lett. 105, 021605 (2014). https://doi.org/10.1063/1.4890110
11. S. C. Cowin, “The viscoelastic behaviour of linear elastic materials with voids,” J. Elasticity 15, 185–192 (1985). https://doi.org/10.1007/BF00041992
12. S. L. Passmann, “Stress relaxation, creep, failure and hysteresis in a linear elastic material with voids,” J. Elasticity 14, 201–212 (1984). https://doi.org/10.1007/BF00041666
13. D. S. Chandrasekharaiah, “Rayleigh–Lamb waves in an elastic plate with voids,” J. Appl. Mech. 54, 509–512 (1987). https://doi.org/10.1115/1.3173061
14. R. J. Atkin, S. C. Cowin, and N. Fox, “On boundary conditions for polar materials,” Z. Angew. Math. Phys. 28, 1017–1026 (1977). https://doi.org/10.1007/BF01601669
15. H. Ramézani, H. Steeb, and J. Jeong, “Analytical and numerical studies on Penalized Micro-Dilatation (PMD) theory: macro-micro link concept,” Eur. J. Mech. A/Solids 34, 130–148 (2012). https://doi.org/10.1016/j.euromechsol.2011.11.002

16. P. L. Bishay, V. Sladek, X. W. Gao, and J. Sladek, “Analysis of elastic media with voids using new mixed-collocation finite element method (MCFEM),” J. Eng. Mech. (2016). https://doi.org/10.1061/(ASCE)EM.1943-7889.0001193
17. J. Sladek, V. Sladek, M. Repka, and P. L. Bishay, “Static and dynamic behavior of porous elastic materials based on micro-dilatation theory: a numerical study using the MLPG method,” Int. J. Solids Struct. 96, 126–135 (2016). https://doi.org/10.1016/j.ijsolstr.2016.06.016
18. J. D. Achenbach, Wave Propagation in Elastic Solids (North-Holland, Amsterdam, 1973).
19. L. N. Trefethen, Spectral Methods in MATLAB (SIAM, Philadelphia, 2000).
20. D. S. Drumheller, “An effect of debonding on stress wave propagation in composite materials,” J. Appl. Mech. 40, 1146–1147 (1973). https://doi.org/10.1115/1.3423156
21. P. Puri and S. C. Cowin, “Plane waves in linear elastic materials with voids,” J. Elasticity 15, 167–183 (1985). https://doi.org/10.1007/BF00041991